Contents lists available at ScienceDirect

International Journal of Heat and Mass Transfer

journal homepage: www.elsevier.com/locate/hmt



Measured spectral, directional radiative behavior of corrugated surfaces



Kyle S. Meaker, Ehsan Mofidipour, Matthew R. Jones, Brian D. Iverson*

Brigham Young University, Provo, UT, 84602, USA

ARTICLE INFO

Article history: Received 26 September 2022 Revised 18 November 2022 Accepted 2 December 2022

Keywords:
Apparent radiative property
Emissivity
Corrugated
V-groove
Spacecraft thermal control

ABSTRACT

Spacecraft thermal control is entirely reliant upon radiative heat transfer with its surroundings for temperature regulation. Current methods are often static in nature and do not provide dynamic control of radiative heat transfer. As a result, modern spacecraft thermal control systems are typically 'cold-biased' with radiators that are larger than necessary for many operating conditions. Deploying a variable radiator as a thermal control technique in which the projected surface area can be adjusted to provide the appropriate heat loss for a given condition can reduce unnecessary heat rejection and reduce power requirements. However, the radiative behavior of the apparent surface representing the expanding/collapsing radiator changes in addition to the projected surface area size. This work experimentally quantifies the spectral, directional emissivity of an apparent surface comprised of a series of V-grooves (e.g. corrugated surface), as a function of angle and highlights its emission characteristics that trend toward black behavior. The experimental setup for quantifying this apparent radiative surface behavior is described and utilized to show the influence of surface geometry, direction and wavelength. Experiments on test samples were performed at 573 K. The experimental design is validated and demonstrated using fully oxidized, nearly diffuse, copper, corrugated test samples. The results presented in this work demonstrate, for the corrugated oxidized copper surfaces tested, that (1) higher emissivity values correspond to higher wavelengths in the spectral range of 2.5 to 15.4 µm (2) apparent emissivity values increase with decreasing V-groove angle resulting in less spectral variation in emissivity and greater blackbody like behavior, (3) azimuth dependence can be relatively small despite the obvious pattern associated with a corrugated surface, and (4) as the V-groove angle decreases, higher emissivity values are associated with $\theta \to 0^\circ$ and $\phi \to 0^\circ$. Results provide a foundation for future radiator design, improved spacecraft thermal control methods, and improved emissivity testing methods for patterned or angular surfaces.

© 2022 Elsevier Ltd. All rights reserved.

1. Introduction

Spacecraft thermal management is a challenging application due to the harsh environment of space, buildup of heat within vital electrical components, and fluctuations in external and internal thermal loads. A particular issue with spacecraft thermal management is that the only method by which excess heat may be rejected is through radiative heat transfer. This is commonly achieved through exterior, extended surfaces known as radiators, which act as static, passive cooling systems with constant geometry and radiative properties [1]. As such, heat rejection varies only according to the relative temperature difference between the internal components of the spacecraft and the surroundings when using a static, passive cooling system.

Static, passive thermal control is widely adopted due to its simplicity in design of specialized radiating surfaces. However, spacecraft radiators are sized sufficiently large such that they are capable of emitting the highest cooling load expected during the lifetime of the spacecraft, a strategy called cold-biasing [2]. With the variable nature of internal and external heat loads during spacecraft operation, cold-biasing results in the use of actively controlled heaters to provide supplementary heating when the heat loss is greater than desired. Such heating scenarios are common and the required additional heating elements, batteries and solar panel capacity conflict with the goal of reduced size, weight and power requirements.

One proposed method to reduce the amount of supplementary heating is through the use of dynamic cooling strategies that provide control in spacecraft emission [3]. Single panel radiators that operate like a gate or shutter in order to conceal or reveal a radiating surface have been explored as a dynamic cooling strategy [4–7]. An example of a powered, multiple-panel, dynamic strat-

^{*} Corresponding author. E-mail address: bdiverson@byu.edu (B.D. Iverson).

Nomenclature Е Emissive power [W m⁻²] **FTIR** Fourier Transform Infrared Spectrometer Height of sample [mm] h Intensity [W m⁻² sr⁻¹] I Normal vector [-] rĩ Ν Number of data sets collected [-] Repeatability [-] r R Response function $[W^{-1} m^2 sr \mu m]$ S Measured signal by FTIR [-] Background compensation function [-] S_0 Temperature [K] Τ Uncertainty [-] 11 V-groove angle [°] γ Emissivity [-] ε θ Polar angle [°] Wavelength [µm] λ Reflectivity [-] ρ ρ'' Bidirectional reflectivity [-] Stefan-Boltzmann constant [W m⁻² K⁻⁴] σ Azimuthal angle [°] Subscripts and superscripts Indicates that [] is an ideal blackbody quantity $[]_b$ Indicates that [] is a laboratory blackbody quantity []_{bb} $[]_d$ Indicates that [] is a diffuse quantity Indicates that [] is an emitted quantity []e Indicates that [] is an incident quantity $[]_i$ $[]_r$ Indicates that [] is a reflected quantity $[]_s$ Indicates that [] is a sample quantity Indicates that [] is a specular quantity $[]_{SD}$ Indicates that [] is a surroundings quantity surr Indicates that [] is a combined specular and diffuse []tot quantity Indicates that [] is directionally dependent $[]_{\theta}$ Indicates that [] is spectrally dependent $[]_{\lambda}$ $[]_{\mu}$ Indicates that [] is an averaged quantity [] Indicates that [] is a hemispherical quantity $[\]'$ Indicates that [] is a directional quantity

egy has also been explored by Mulford et al. [8], where the turn-down ratio (or fraction of largest possible emitted energy to smallest possible emitted energy) of an actively controlled radiator was determined. The multiple panels considered by Mulford et al. collapsed and expanded to provide an appropriate amount of heat loss for given operating and environmental conditions. The changing geometry results in a variable apparent emissivity (spectral, directional emissivity of the representative surface for the collapsing, multiple-panel radiator) which depends on radiator panel positioning, wavelength, and direction. One contribution of the current work is to demonstrate the directional behavior of emission from multiple panel radiators (e.g. corrugated surfaces) for varying geometrical conditions.

1.1. Apparent surfaces

Emission and absorption of multiple panel radiators is altered by the fact that surfaces that comprise such a radiator are seen by other surfaces comprising the radiator. These effects can be combined into an apparent surface behavior representing the area formed by the collection of cavities comprising the multiple-surface radiator. For corrugated surfaces or origami-inspired surfaces [8–12], these cavity openings are repeating in nature. When the vertices associated with the cavity openings all lie in the same

plane, the apparent surface is a 2D plane representing the cavity openings (see Fig. 1).

Introducing a surface representing a series of cavities enables the specification of radiative properties for the "apparent" radiative behavior of a surface comprised of these cavities. Further, apparent surfaces comprised of cavities are unique in that their emissivity depends not only on material properties but also on the geometry of the cavities which comprise it, allowing variable control of the apparent emissivity through variation of cavity geometry. Such control was demonstrated in previous work where the relationship between measured thermal radiation and a collapsing radiator was established experimentally [8,13]. However, previous works only considered total, hemispherical apparent surface behavior. Understanding the effects of geometry on the spectral, directional radiative behavior is explored in this work through measurement of the radiative behavior of corrugated surfaces. Corrugated geometries are amenable to modeling, achievable with accessible manufacturing methods, and can be validated with previous V-groove studies for simplified conditions.

Fully specifying the emission from a planar surface requires quantifying the spectral, directional emissivity $\varepsilon_{\lambda,\theta}$. The spectral, directional emissivity is the ratio of the emitted spectral intensity of a surface $I_{\lambda,\theta,e}$ and the spectral intensity of a blackbody $I_{\lambda,b}$ at the same temperature.

$$\varepsilon_{\lambda,\theta}(\lambda,T,\theta,\phi) \equiv \frac{I_{\lambda,\theta,e}(\lambda,T,\theta,\phi)}{I_{\lambda,b}(\lambda,T)} \tag{1}$$

 $I_{\lambda,\theta,e}$ is the rate at which radiant energy is emitted at wavelength λ in the (θ,ϕ) direction (see Fig. 1) per unit area of the emitting surface normal to this direction, per unit solid angle about this direction, and per unit wavelength interval about λ . Understanding the directional dependence of the apparent emissivity is an important step in developing techniques for dynamic control of apparent radiative surface properties and affecting radiative heat transfer through surface orientation. For example, this understanding could be used to minimize or maximize solar absorption or emission as needed, for thermal control.

1.2. Spectral, directional emissivity

Multispectral radiation thermometry and its contactless measurement approach have enabled an increasing amount of surface property characterization in recent years [14-19]. The spectral, normal emissivity has been investigated for a number of surfaces and materials, often limited to some spectral range associated with the detector of the measurement device [14.15.20-28]. Additionally, many have investigated methods to measure the spectral, directional emissivity of nominally flat surfaces, though generally only for surfaces in which the variation in ϕ was neglected (weak emissivity dependence on the azimuthal angle is typically due to random orientation of grains in most surfaces making this approximation appropriate [29]). Wang et al. heated a stainless steel 330 sample using electromagnetic induction in an atmosphere controlled apparatus (water cooled chamber capable of supporting various testing environments, e.g. vacuum) and performed directional measurements over the range $0 \le \theta \le 86^{\circ}$ in a spectral band of 2 - 6 µm [30]. A simpler experimental setup was built by Yu et al. that did not rely on an enclosed, controlled environment but provided a broad directional measurement range (0 $\leq \theta \leq$ 82°) over a limited spectral range (0.95 - 1.60 µm) due to the use of a visible light spectrometer [31]. Teodorescu et al. incorporated an FTIR spectrometer into their experimental setup, allowing for a larger wavelength range of measurement (2 – 20 μ m), though their directional measurement apparatus was limited to 0 - 72° measured at 6° increments [32]. Improved fidelity in angle measurement was achieved by Guo et al. through the use of a computer

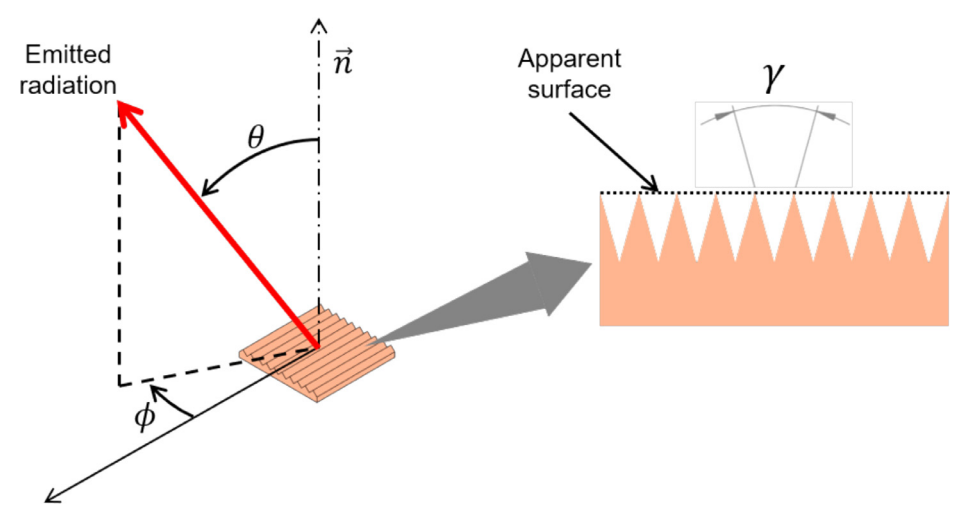


Fig. 1. Hemispherical coordinate system and nomenclature for an apparent surface comprised of cavity openings all lying in the same plane resulting in a 2D apparent surface.

controlled rotary stage with a resolution of 0.01° while still employing an FTIR spectrometer to provide a wide wavelength span (1.28 – 28.6 μm), though over a slightly smaller directional range (0 $\leq \theta \leq$ 60°) [33]. Del Campo et al. achieved a high fidelity angle measurement (through use of a stepper motor) while maintaining a broad directional and spectral range (0 $\leq \theta \leq$ 80° and 1.28 – 25 μm) in a controlled atmosphere [34]. As noted above, existing literature has largely neglected directional dependence on ϕ , with all directional measurements made by varying θ alone (see also Fig. 1). For previous studies, this was sufficient due to the assumption of constant emissivity in the ϕ direction for the surfaces investigated.

Little work has been done to measure the emissivity of apparent surfaces comprised of repeating angular cavities, with existing literature limited to determining the total, hemispherical emissivity [8,11,13,35,36]. As previous spectral, directional emissivity measurement techniques were not capable of determining dependence on ϕ , a methodology that is capable of measuring the spectral, directional emissivity of a surface comprised of angular cavities would be valuable as reference data for validation of approaches that seek to capitalize on the directional behavior of apparent surfaces for net radiation heat transfer.

1.3. Problem statement

This work develops a methodology to experimentally measure the apparent spectral, directional emissivity of complex surfaces. The methodology is applied to determine the directional radiative surface properties of a multi-panel, corrugated radiator comprised of repeating V-groove cavities. This directional dependence is presented to highlight the significant variance in apparent radiative behavior of corrugated angular surfaces (e.g. origami inspired surfaces) and enable designers to utilize preferred directions of emission and absorption to control radiative heat transfer. A corrugated surface was selected as the demonstration geometry as it is amenable to future modeling, is achievable with accessible manufacturing methods and since the surface simplifies to a single V-groove for which previous studies can apply.

2. Methods

Directional emission behavior of corrugated surfaces was explored using multiple surfaces of varying V-groove angle as discussed in Section 2.1. The spectral, directional emissivity of each

surface was determined by comparing the spectral intensity of a sample in a given direction and at a given temperature with that of a blackbody at the same temperature. Efforts to account for any effects on the measured signal due to attenuation of the emitted radiation as well as radiation incident on the detector from the surroundings is found in Section 2.2.1. We report in Section 2.2.2 a measurement system capable of providing (1) directional control of the position of the detector on the hemisphere above the sample surface; (2) a method of heating the sample in a controlled manner to produce a strong and stable signal; (3) a detector that is sensitive to signals in the mid-IR range; and (4) a blackbody that can be heated to the same temperature as the sample. Before producing the desired data for the prepared samples of interest, the experiment was validated (Section 2.2.5) by measuring two known quantities, namely the spectral intensity of a blackbody at a specified temperature (given by the Planck distribution) and the spectral, normal emissivity of stably oxidized, highly polished copper (tabulated and published results easily obtained for comparison). Additionally, while performing the core data collection for the three copper samples, repeat measurements for each sample were made in order the determine the uncertainty associated with the results (Section 2.2.4).

2.1. Sample characteristics and control

A corrugated surface, comprised of a repeating pattern of V-grooves, was selected to demonstrate the directional emission behavior of surfaces comprised of cavity emission. Three sample surfaces were prepared, as shown below in Fig. 2. A second flat sample, identical to that shown below, was also prepared and polished for the purpose of validation. All surfaces were supplied by Central Utah Tool (centralutahtool.com).

Sample surfaces were machined out of C110 copper bar stock (5.08 cm by 5.08 cm), which has a purity of 99.9% and a conductivity of 401 W m $^{-1}$ K $^{-1}$. The top surface of each sample was precisely machined using wire EDM to achieve the corrugation with minimal rounding at the bottom of the V-groove valley. Surface roughness testing of the flat sample was performed, which reported an Ra value of 0.566 μ m (Table 1). Four equally spaced cartridge heater holes were bored into each sample, with three smaller holes being spaced between the cartridge holes for thermocouples (as shown in Fig. 3). Thermocouples provided feedback temperature control, as well to ensure temperature uniformity. A summary of the sample conditions is given in Table 1. The flat,



Fig. 2. Fabricated copper samples used to model a radiator over various degrees of folding. The top surface of the flat sample was also machined using the same process used to produce the folded surfaces, namely, wire EDM.

Table 1Sample specifications and geometry. V-groove surfaces were assumed to have the same surface roughness as the flat, nearly diffuse sample since their surface finishing procedure was the same.

Sample	Height (h)	Angle (γ)	Surface Roughness (Ra)
Flat, Nearly Diffuse	12.70 mm	180°	0.566 μm
Flat, Nearly Specular V-groove 1	12.70 mm 18.97 mm	180° 30.93°	0.047 μm 0.566 μm
V-groove 2	18.13 mm	14.83°	0.566 μm

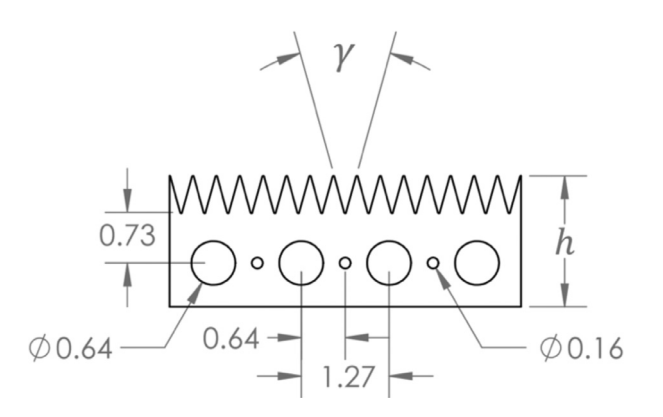


Fig. 3. Side profile of a sample surface with dimensions corresponding to values listed in Table 1 (in cm). The 0.16 cm diameter holes were used for thermocouples, while the 0.64 cm diameter holes were used for cartridge heaters.

nearly diffuse sample was produced to represent a corrugated radiator in a fully open position.

A fourth flat surface, that was polished to achieve specular behavior after cutting to the desired size, was produced with the same polishing methods as those outlined in comparative literature [37,38]. Surface roughness testing was also performed for this sample, which was found to have an Ra value of $0.047 \mu m$ (Table 1).

The height of each sample was designed so that the minimum distance between the cartridge heaters and exposed sample surface would be constant between each sample (top surface of flat samples or V-groove bottom for corrugated samples). V-groove angles were selected based on reasonable machining capability while also providing an intermediate position relative to a flat sample. Additionally, for both V-groove samples, the angles were chosen such that a cavity would lie at the center of the sample, since the cavity effect was of interest during testing and the design of the setup meant that the detector would view the center of the sample when placed in the experiment apparatus. Finally, the angles were also adjusted so that only whole cavities would exist in the sample designs.

The heaters and thermocouples were evenly spaced from each other to ensure temperature uniformity (Fig. 3) with the center thermocouple being used for the thermal control system feedback.

These thermocouples were measured to be within \pm 1 K of each other during testing. Additional assurance of temperature uniformity was obtained with infrared imaging from the side of each sample at the operating temperature of 573 K. Representative results plotted at the base of the V-grooves for sample V-groove 2 indicate a standard deviation of 2.6 K (see Supplementary Material, Sample Temperature Uniformity).

Heating of the samples occurred using a SOLO basic single loop PID temperature controller assembled with four cartridge heaters (McMaster-Carr, Part 3618K412 in series and a type K thermocouple (Omega, Part HTTC36-K-116U-1.5) for feedback. In order to limit the amount of heat transfer occurring between the sample and testing apparatus, a 0.32 cm thick composite insulation (McMaster-Carr insulation sheet 9323K11; thermal conductivity of 0.005 W m⁻¹ K⁻¹ calculated using the thickness and reported Rvalue of 0.6) with a maximum rated temperature of 866 K was placed between the sample mount and the small rotating stage (as shown in Fig. 4a) used to control rotation in ϕ . Gains were adjusted within the control system until a stability of ± 1 K was achieved for the control thermocouple. Additionally, the temperature of the lab was maintained at approximately 293 K using the HVAC system, with humidity reduced to below 30% using a dehumidifier.

2.2. Spectral, directional emissivity

Development of the method to determine spectral, directional emissivity consisted of a model to relate measurable quantities with spectral, directional emissivity and designing/constructing a validated experimental apparatus. These topics are addressed in Sections 2.2.1 through 2.2.5.

2.2.1. Emissivity Model

An FTIR (ThermoFisher 8700 spectrometer) with an MCT liquid nitrogen cooled detector and KBr beam splitter was used to measure emission from sample surfaces. The intensity incident on the port $(I_{\lambda,i})$ results in a signal from the detector $(S_{\lambda,\theta,s})$. In the case of this experiment, the intensity incident on the port is comprised of the intensity emitted and reflected from the sample surface in a given direction after the intensity has been attenuated by the experimental setup, participating medium, reflectivity of the optical path, etc. (see Figs. 4b and 5a). Additionally, background radiation (originating from sources other than a sample of interest) also contributes to the spectral intensity incident on the detector port. Therefore, the signal generated by the FTIR is proportional to a combination of the attenuated intensity emitted and reflected from the sample and the background radiation, as follows.

$$S_{\lambda,\theta,s} = R(\lambda) \left[I_{\lambda,\theta,e}(T_s) + I_{\lambda,\theta,r}(T_{surr}) \right] + S_0(\lambda)$$
 (2)

Changes or attenuation to the spectral intensity of the sample that occur in the optical path are modeled in the response function $R(\lambda)$. The signal associated with background radiation is mod-

(a) Sample Positioning Assembly (b) Mirror Mount Assembly Small Rotating Translating Stage Stage 1 Rotating Sample Kinematic Mirror 909 Mount Mount Parabolio Mirror Optical Goniometer Post Translating Post Square Mount Mount Large Rotating 50 mm Stage Optical Rail

Fig. 4. (a) Side view of Sample Positioning Assembly, with angles θ and ϕ controlled using the rotating stages shown. (b) Side view of the Mirror Mount Assembly for the parabolic mirror used to collimate sample and blackbody data.

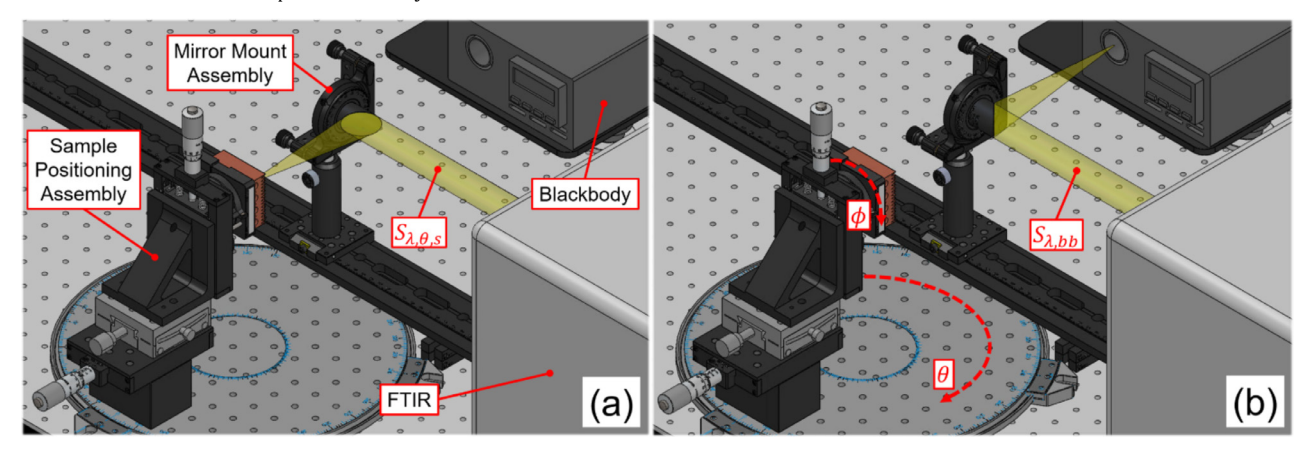


Fig. 5. Assembly diagram of the spectral, directional emissivity experiment with isometric views for measuring (a) sample signal $S_{\lambda,\theta,s}$, and (b) blackbody signal $S_{\lambda,bb}$. Note that directional control of ϕ and θ are shown in (b).

eled in the background compensation function $S_0(\lambda)$. For a non-blackbody sample, the spectral intensity is the emitted spectral intensity from the sample (assuming uniform sample temperature) combined with the reflected irradiation associated with the surroundings (assuming isothermal surroundings).

$$S_{\lambda,\theta,s} = R(\lambda) \left[\varepsilon_{\lambda,\theta,s}(\lambda, T_s, \theta, \phi) I_{\lambda,b}(\lambda, T_s) + \rho_{\lambda,s}^{\triangle'} \right]$$

$$(\lambda, T_s, \theta, \phi) \varepsilon_{\lambda,\theta,surr}(\lambda, T_{surr}, \theta, \phi) I_{\lambda,b}(\lambda, T_{surr}) + S_0(\lambda)$$
(3)

Here, $S_{\lambda,\theta,s}$ is the signal associated with the sample being tested at a given wavelength, $\varepsilon_{\lambda,\theta,s}(\lambda,T_s,\theta,\phi)$ is the spectral, directional emissivity of the sample, $I_{\lambda,b}(\lambda,T_s)$ is the spectral intensity of an ideal blackbody as predicted by Planck's Distribution at the temperature of the sample, $\rho_{\lambda,s}^{e,f}(\lambda,T_s,\theta,\phi)$ is the spectral, hemispherical-directional reflectance of the sample, $\varepsilon_{\lambda,\theta,surr}(\lambda,T_{surr},\theta,\phi)$ is the spectral, directional emissivity of the surroundings, and $I_{\lambda,b}(\lambda,T_{surr})$ is the spectral intensity of an ideal blackbody as predicted by Planck's distribution at the temperature of the surroundings.

For a signal provided by a blackbody source (such as the laboratory blackbody shown in Fig. 5), since there is no reflected irradiation, the equation above simplifies to the following,

$$S_{\lambda,bb} = R(\lambda)\varepsilon_{bb}I_{\lambda,b}(\lambda, T_{bb}) + S_0(\lambda) \tag{4}$$

where $S_{\lambda,bb}$ is the signal from a laboratory blackbody, ε_{bb} is the total, hemispherical emissivity of the laboratory blackbody (assuming

 ε_{bb} < 1), and $I_{\lambda,b}(\lambda,T_{bb})$ is the spectral intensity of an ideal blackbody as predicted by the Planck distribution at the temperature of the laboratory blackbody.

The response function and background compensation function can then be quantified by performing measurements of the laboratory blackbody signal at two different temperatures.

$$S_{\lambda,bb1} = R(\lambda)\varepsilon_{bb}I_{\lambda,b}(\lambda, T_{bb1}) + S_0(\lambda)$$
(5)

$$S_{\lambda,bb2} = R(\lambda)\varepsilon_{bb}I_{\lambda,b}(\lambda, T_{bb2}) + S_0(\lambda) \tag{6}$$

Eqs. (5) and (6) are a two-equation, two-unknown $(R(\lambda))$ and $S_0(\lambda)$ system which can be solved for the response function and background compensation function using the measured laboratory blackbody signals and known emissivity and spectral intensities, as follows.

$$R(\lambda) = \frac{S_{\lambda,bb1} - S_{\lambda,bb2}}{\varepsilon_{bb} \left[I_{\lambda,b}(\lambda, T_{bb1}) - I_{\lambda,b}(\lambda, T_{bb2}) \right]}$$
(7)

$$S_0(\lambda) = \frac{S_{\lambda,bb2}I_{\lambda,b}(\lambda, T_{bb1}) - S_{\lambda,bb1}I_{\lambda,b}(\lambda, T_{bb2})}{I_{\lambda,b}(\lambda, T_{bb1}) - I_{\lambda,b}(\lambda, T_{bb2})}$$
(8)

Returning to Eq. (3), since the surroundings of the experiment are large and approximately isothermal, the surroundings can be modeled as a blackbody at T_{surr} . This approximation results in $\varepsilon_{\lambda,\theta,surr} \approx 1$ over all wavelengths and directions, and also means

that the surface is diffusely irradiated. Therefore, in accordance with the literature, the following is true [29].

$$\rho_{\lambda_s}^{\alpha'}(\lambda, T_s, \theta, \phi) = \rho_{\lambda_s}^{\prime \alpha}(\lambda, T_s, \theta, \phi) \tag{9}$$

In other words, the spectral, hemispherical-directional reflectivity is equal to the spectral, directional-hemispherical reflectivity. If a given sample is an opaque surface (true for all surfaces in the current work), the following also is true.

$$\varepsilon_{\lambda,\theta,s}(\lambda,T_s,\theta,\phi) = 1 - \rho_{\lambda,s}^{\prime a}(\lambda,T_s,\theta,\phi) \tag{10}$$

Thus, Eq. (3) becomes,

$$S_{\lambda,\theta,s} = R(\lambda) \left[\varepsilon_{\lambda,\theta,s}(\lambda, T_s, \theta, \phi) I_{\lambda,b}(\lambda, T_s) + \left(1 - \varepsilon_{\lambda,\theta,s}(\lambda, T_s, \theta, \phi) \right) I_{\lambda,b}(\lambda, T_{surr}) \right] + S_0(\lambda).$$
(11)

Solving for $\varepsilon_{\lambda,\theta,s}(\lambda,T_s,\theta,\phi)$, we obtain the following.

$$\varepsilon_{\lambda,\theta,s}(\lambda,T_s,\theta,\phi)$$

$$= \frac{S_{\lambda,\theta,s} - S_{\lambda,bb} + R(\lambda) \left[\varepsilon_{bb} I_{\lambda,b}(\lambda, T_s) - I_{\lambda,b}(\lambda, T_{surr}) \right]}{R(\lambda) \left[I_{\lambda,b}(\lambda, T_s) - I_{\lambda,b}(\lambda, T_{surr}) \right]}$$
(12)

Here, emissivity is dependent upon wavelength and direction, as desired. Calculation of the total, directional emissivity requires weighted integration of the spectral, directional emissivity, using the spectral blackbody emissive power as follows.

$$\varepsilon_{\theta,s}(T_s,\theta,\phi) = \frac{1}{\sigma T_s^4} \int_0^\infty \varepsilon_{\lambda,\theta,s}(\lambda,T_s,\theta,\phi) E_{\lambda,b}(\lambda,T_s) d\lambda \tag{13}$$

Therefore, by first determining the response function (measured during each test) and then measuring the sample and laboratory blackbody signal at the same temperature (T_s), one can determine the spectral, directional emissivity and total, directional emissivity of a sample surface from measured FTIR signals associated with a surface of interest and a laboratory blackbody reference. This approach is developed and used in the literature to measure the spectral, directional emissivity of various surfaces, though often applied to surfaces where no variation in ϕ was assumed [31,34].

Comparison of the magnitude of both terms in Eq. (2), namely the attenuated signal from the sample, $R(\lambda)[I_{\lambda,\theta,e}(T_S)+I_{\lambda,\theta,r}(T_{surr})]$, and the background compensation function, $S_0(\lambda)$, was performed for the flat, nearly diffuse sample in the normal direction. Additionally, a comparison of the response functions and background compensation functions obtained for each test was performed. These results are contained in Supplementary Material.

2.2.2. Experimental setup

To determine the spectral, directional emissivity in any direction of the hemisphere above a sample surface, the sample positioning assembly is fitted with two rotating stages allowing position changes in ϕ and θ (Fig. 4a). This approach in altering the orientation of the sample, as opposed to moving the detector for measurement, is preferred when changing the position of the detector is not feasible. Here, the optical path for measurement remains fixed while the sample rotates.

The Sample Positioning Assembly provides precise control over the location and orientation of the sample using two translating stages and a goniometer (Fig. 4a). The location and orientation of the parabolic mirror is also precisely controlled with a kinematic mount and rotating stage (Fig. 4b). This parabolic mirror is used to redirect and collimate the radiation into the FTIR from either the sample (Fig. 5a) or blackbody (Fig. 5b). Fig. 6 illustrates the mirror location indicating that the mirror and sample are aligned such that the parabolic mirror is focused on the center of the apparent surface of the V-groove located in the center of the sample.

To determine the response function and background compensation function, a spectral signal from a laboratory blackbody (552 Quickcal R Blackbody) is obtained at two temperatures $(S_{\lambda,bb1}, S_{\lambda,bb2})$ in the assembly configuration of Fig. 5b using the FTIR detector. For the blackbody, a reported value of $\varepsilon_{bb}=0.99$ was used. With the spectral intensity of a blackbody specified $I_{\lambda,b}(\lambda,T_{bb})$ according to Planck's distribution at $T_{bb1}=568$ K and $T_{bb2}=578$ K (5 K above and below the target sample temperature of 573 K), Eqs. (7) and (8) were used to calculate the response function and background compensation function. The laboratory blackbody was allowed to reach steady state behavior over 15 min with less than 0.2 K variation in temperature with time.

In order to determine the spectral, directional emissivity, a sample surface is affixed to the sample positioning assembly (Figs. 4a and 5a), oriented to a desired direction and allowed to reach the desired setpoint temperature of 573 K over 30 min. Steady state was determined to be when the sample temperature varied less than ± 2 K over 10 min. This variation in temperature was taken to be the uncertainty in temperature associated with the sample. Spectral signals from the sample were then collected as the sample rotated through various positions, with θ varying from -80° to 80° in 20° increments and ϕ varying from 0 to 90° in 30° increments. The resulting data, comprised of 36 distinct data sets corresponding to 36 angle pairs, is then processed by calculating the spectral emissivity in each direction where measurements were made. This calculation is performed with Eq. (12) using sample data collected in a given direction $(S_{\lambda,\theta,s})$, measured blackbody data at the same temperature as the sample $(S_{\lambda,bb})$, and the empirically determined response function and background compensation function. The result is 36 data sets for emissivity in a given direction, each as a function of wavelength. The average emissivity over the spectral range is also calculated for each data set (i.e. direction). Spectrally dependent and spectrally integrated (total) data for a given direction are identified and reported in the results section.

2.2.3. Uncertainty analysis

The square of the uncertainty for a calculated dependent variable is equal to the sum of the square of each independent variables' uncertainty multiplied by the partial derivative of the dependent variable with respect to that independent variable. In this manner, the uncertainty associated with spectral, directional emissivity (Eq. (12)) was determined for each measured direction and wavelength.

$$\Delta \varepsilon_{\lambda,\theta,s}^{2} = \left(\frac{\partial \varepsilon_{\lambda,\theta,s}}{\partial S_{\lambda,\theta,s}} \Delta S_{\lambda,\theta,s}\right)^{2} + \left(\frac{\partial \varepsilon_{\lambda,\theta,s}}{\partial S_{\lambda,bb}} \Delta S_{\lambda,bb}\right)^{2} + \left(\frac{\partial \varepsilon_{\lambda,\theta,s}}{\partial R} \Delta R\right)^{2} + \left(\frac{\partial \varepsilon_{\lambda,\theta,s}}{\partial \varepsilon_{bb}} \Delta \varepsilon_{bb}\right)^{2} + \left(\frac{\partial \varepsilon_{\lambda,\theta,s}}{\partial I_{\lambda,b}(\lambda, T_{s})} \frac{\partial I_{\lambda,b}(\lambda, T_{s})}{\partial T_{s}} \Delta T_{s}\right)^{2} + \left(\frac{\partial \varepsilon_{\lambda,\theta,s}}{\partial I_{\lambda,b}(\lambda, T_{surr})} \frac{\partial I_{\lambda,b}(\lambda, T_{surr})}{\partial T_{surr}} \Delta T_{surr}\right)^{2}$$

$$(14)$$

The derivatives of $\varepsilon_{\lambda,\theta,s}$ were evaluated using Eq. (12) and the intensity derivatives were evaluated using the Planck distribution. In order to evaluate the uncertainty associated with the response function, ΔR , a similar analysis was performed for Eq. (7), as follows.

$$\Delta R^{2} = \left(\frac{\partial R}{\partial S_{\lambda,bb1}} \Delta S_{\lambda,bb1}\right)^{2} + \left(\frac{\partial R}{\partial S_{\lambda,bb2}} \Delta S_{\lambda,bb2}\right)^{2} + \left(\frac{\partial R}{\partial \varepsilon_{bb}} \Delta \varepsilon_{bb}\right)^{2} + \left(\frac{\partial R}{\partial I_{\lambda,b}(\lambda, T_{bb1})} \Delta T_{bb1}\right)^{2} + \left(\frac{\partial R}{\partial I_{\lambda,b}(\lambda, T_{bb2})} \frac{\partial I_{\lambda,b}(\lambda, T_{bb2})}{\partial T_{bb1}} \Delta T_{bb1}\right)^{2} + \left(\frac{\partial R}{\partial I_{\lambda,b}(\lambda, T_{bb2})} \frac{\partial I_{\lambda,b}(\lambda, T_{bb2})}{\partial T_{bb2}} \Delta T_{bb2}\right)^{2}$$

$$(15)$$

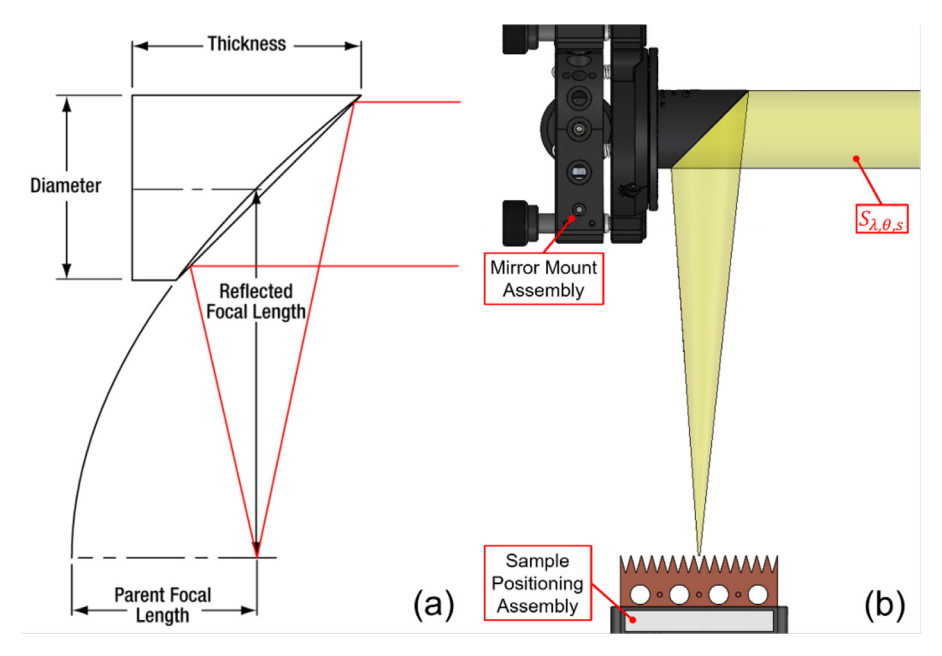


Fig. 6. Top down views demonstrating the interrogation region of the sample surface including a (a) schematic design of the parabolic mirror and location of the focus (used with permission from Thorlabs, Inc., part number MPD169-P01) and (b) the experimental setup with sample and mirror mount assemblies. Component positioning is such that the mirror is focused on the center of the apparent surface of the V-groove located in the center of the sample.

 Table 2

 Uncertainty terms with their associated values or methods.

Uncertainty	Value or Method
$\Delta S_{\lambda,\theta,s}$	Determined as the standard deviation of $S_{\lambda,\theta,s}$ over repeat tests
$\Delta S_{\lambda,bb}$	Determined as the standard deviation of $S_{\lambda,bb}$ over repeat tests
ΔR	Determined as the standard deviation of R using Eq. (15)
$\Delta arepsilon_{bb}$	± 0.005 from blackbody manufacturer Quickcal
$\Delta T_{\rm s}$	± 1 K from control system manufacturer SOLO
ΔT_{surr}	± 0.3 K from temperature meter manufacturer BFOUR
$\Delta S_{\lambda,bb1}$	Determined as the standard deviation of $S_{\lambda,bb1}$ over repeat tests
$\Delta S_{\lambda,bb2}$	Determined as the standard deviation of $S_{\lambda,bb2}$ over repeat tests
ΔT_{bb1}	± 0.1 K from blackbody manufacturer Quickcal
ΔT_{bb2}	± 0.1 K from blackbody manufacturer Quickcal

The derivatives of ΔR were evaluated using Eq. (7). Uncertainties for each variable appearing in Eqs. (14) and (15) and the methods used to obtain or determine them are summarized in Table 2.

2.2.4. Repeatability analysis

Repeatability associated with spectral, directional emissivity measurements was determined by performing repeat testing on each sample shown in Fig. 2. Three identical tests were performed per sample, providing three data sets for each measured direction. Repeatability (r) in reported spectral, directional emissivity values was calculated using the standard deviation between data sets

$$r_{\lambda,\theta} = \sqrt{\frac{\sum \left(\varepsilon_{\lambda,\theta} - \varepsilon_{\lambda,\theta,\mu}\right)^2}{N}} \tag{16}$$

where $r_{\lambda,\theta}$ is the repeatability associated with a measured direction and wavelength, $\varepsilon_{\lambda,\theta}$ is the emissivity in a measured direction with an associated wavelength, $\varepsilon_{\lambda,\theta,\mu}$ is the average of all emissivities in a measured direction at a given wavelength, and N is the number of data sets collected for a measured direction and wavelength. Additionally, each time testing was performed, θ was varied from -80° to 80° (as opposed to 0 to 80°), providing replicate data relative to $\theta=0^\circ$. Given the symmetrical design of each sample, spectral emissivity in a measured direction is expected to agree with the value obtained at the accompanying angle of sym-

metry, with any difference due to the repeatability of the measurement method. Therefore, six data sets for each direction were used to calculate the repeatability. For all data presented in the results section, average repeatability values for each test performed (indicating a standard deviation among repeat measurements) are below 0.02; these low values indicate high repeatability with excellent agreement from measurement to measurement.

2.2.5. Experiment validation

Validation of the spectral, directional emissivity experiment consisted of three main tasks: (1) measurement of the spectral intensity of a laboratory blackbody using the blackbody measurement assembly of Fig. 5b for comparison with the Planck distribution; (2) measurement of the spectral, normal emissivity of a polished, flat, stably oxidized copper sample at 573 K and comparison with comparable conditions reported in the literature; and (3) measurement of the spectral emissivity of silicon carbide (SiC) at 220°C with comparison data from the literature.

The first validation task was accomplished by measuring the response function and background compensation function as outlined above using Eqs. (7) and (8). Rearranging Eq. (4), it was then possible to determine the spectral intensity of a blackbody using the response function, background compensation function, and measured spectral signal from the blackbody at an operating temperature of 573 K. Results of the first validation effort are shown in Fig. 7. Agreement between the Planck distribution at 573 K and the measured spectral intensity of the laboratory blackbody set at 573 K can be seen in the two data sets; the average percent difference was 0.056%, indicating excellent agreement.

The second validation task involved the same procedure described in Section 2.2.2 (measuring the spectral, directional emissivity) but examining the spectral signal in the normal direction ($\theta=0$ and $\phi=0$). Consistent with other surfaces in the literature, a flat copper sample was highly polished using a palm sander, sanding lubricant, and sandpaper (progressively through 400, 800, 1500, and 2000 grit) then heated to become stably oxidized [37,38]. To achieve stable oxidation, the sample was heated for 10.5 hours before measurement, with the heating time deter-

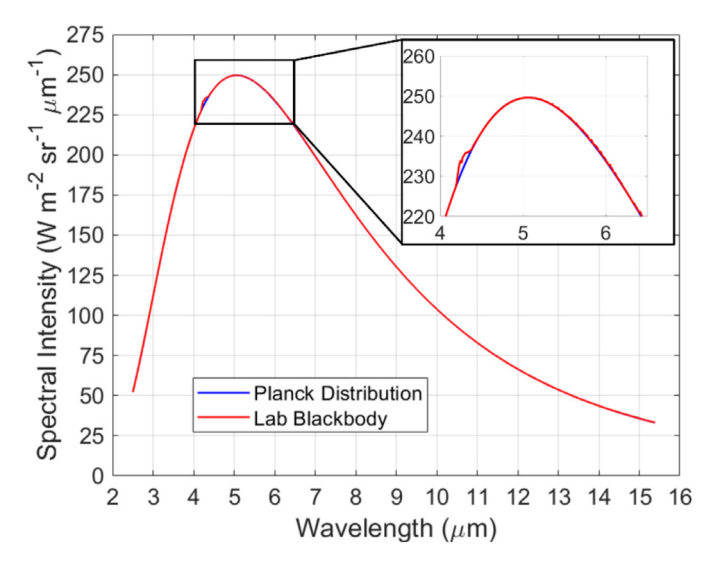


Fig. 7. Comparison of the measured spectral intensity of the laboratory blackbody to that predicted by the Planck distribution.

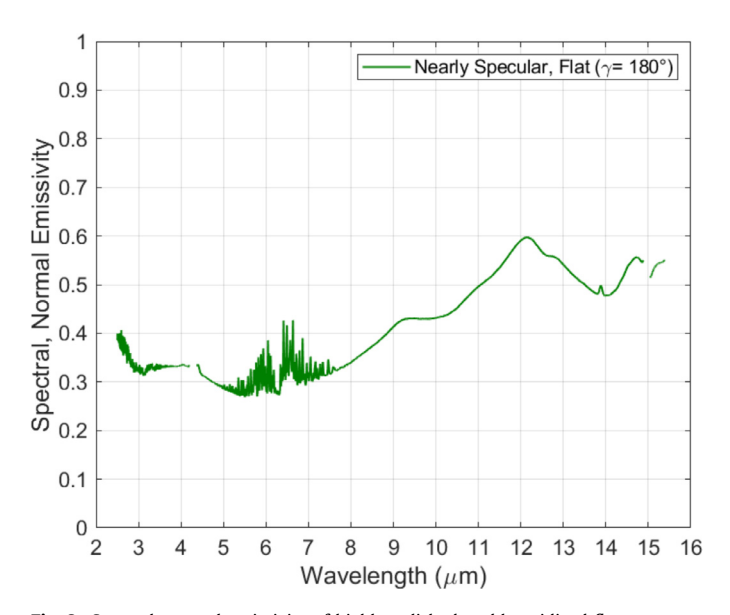


Fig. 8. Spectral, normal emissivity of highly polished, stably oxidized flat copper at 573 K. The average emissivity over the measurable wavelength range is 0.42, with a maximum of 0.64 at a wavelength of 14.97 μ m and a minimum of 0.27 at a wavelength of 5.51 μ m.

mined by comparing measured signals taken every 30 min until negligible changes between spectral signals were observed.

Results from the second validation task are shown in Fig. 8, where the normal emissivity of highly polished, stably oxidized copper at 573 K is plotted as a function of wavelength. Anomalous peaks at 4.3 and 15 µm correspond with significant drops in the measured FTIR signals $(S_{\lambda \theta s})$ at these CO_2 absorption wavelengths; data in these regions is omitted from Fig. 8. Similar peaks were also reported in comparison literature [37], and is likely not associated with the surface emission. Further, noise in the spectral regions <3 μm and between 5.5 – 7.5 μm is due to water vapor absorption. An average value emissivity of 0.42 was obtained over the entire measured wavelength range. A total, hemispherical emissivity of 0.50 is reported for highly polished, stably oxidized copper at 600 K, representing a 16% difference [38]. This discrepancy is likely due, at least in part, to the fact that emissivity was obtained at an elevated temperature relative to the current work (difference of 27 K), especially since emissivity is shown to increase with temperature. Peaks in the measured signal are affected by the thickness and dielectric characteristics of the oxide layer, as well as surface roughness [37].

Additionally, Yu et al. measured the spectral, normal emissivity of copper during the process of oxidation at 573, 673, 773, and 873 K [37]. Although one temperature matches with our test condition a 573 K, some differences in testing conditions exist between the current work and that reported by Yu et al. Samples were heated for up to 60 min at temperature (as opposed to 10.5 hours in the current work), with emissivity measurements made at 10 min increments. Although Yu et al. also employed an FTIR (a Bruker 70V) for measurement, a less sensitive, thermoelectrically cooled DTGS detector was used as opposed to the liquid-nitrogen-cooled, MCT detector used in the current work. Nevertheless, Yu et al. reported a 0.421 normal emissivity for copper after 60 min of oxidization at 573 K at a wavelength of 9 μm ; this agrees well with the measured value of 0.413 at 9 µm for the current oxidation conditions. In light of the experimental differences mentioned above, some disagreement may be expected. However, the wavelength of 9 µm for comparison was selected in a range where little noise was present in measured data. Such agreement in reproducing blackbody behavior and reported emissivity values gives confidence in the experimental approach and corresponding data.

The third validation task was similar to the oxidized copper sample above. However, the spectral emissivity was obtained for silicon carbide in two different configurations, with good agreement relative to published data. Details for this measurement and comparison are provided in Supplementary Material.

3. Results

The methods described above were used to produce spectral, directional emissivity results for each sample surface. In Section 3.1, spectral variations are considered by comparing the spectral, normal emissivity of each sample surface. Directional effects at a constant wavelength (10.38 μ m, corresponding to the most diffuse distribution at $\phi=0^\circ$ for the flat, nearly diffuse sample) are presented in Section 3.2 as well as directional effects observed when integrated over the entire spectral range measured (2.5 to 15.4 μ m) in Section 3.3. Section 3.4 considers the effect of both directional and spectral variation by allowing wavelength and θ to vary while ϕ is held constant at 90°. Notable trends are mentioned in each section, with further discussion provided in Section 4. Uncertainty values are summarized in figure captions.

3.1. Effects of surface geometry on spectral, normal emissivity

The spectral, normal emissivity of each sample surface is presented in Fig. 9, with corresponding uncertainty summarized in the figure caption. As shown in the figure, with decreasing V-groove angle γ , a clear increase in emissivity over the entire measured spectral range is apparent. This increase in spectral, normal emissivity is consistent with the behavior of a V-groove; as the cavity opening of the V-groove decreases, it behaves more like a blackbody. Further, as the spectral, normal emissivity approaches unity, the spectral distribution becomes more constant over the measured wavelength range. For each surface, the highest spectral emissivity values correspond with longer wavelengths.

The influence of water vapor and CO_2 absorption bands is also present in Fig. 9. Water vapor absorption is observed in the spectral regions $< 3 \mu m$ and from $5.5 - 7.5 \mu m$. The effect of CO_2 absorption is also observed at 4.3 and 15.0 μm ; these anomalies are consistent with results reported in prior literature [39]. Finally, a peak is observed in the results for each sample surface at approximately 9.2 μm ; this peak was also observed by Yu et al. and is a

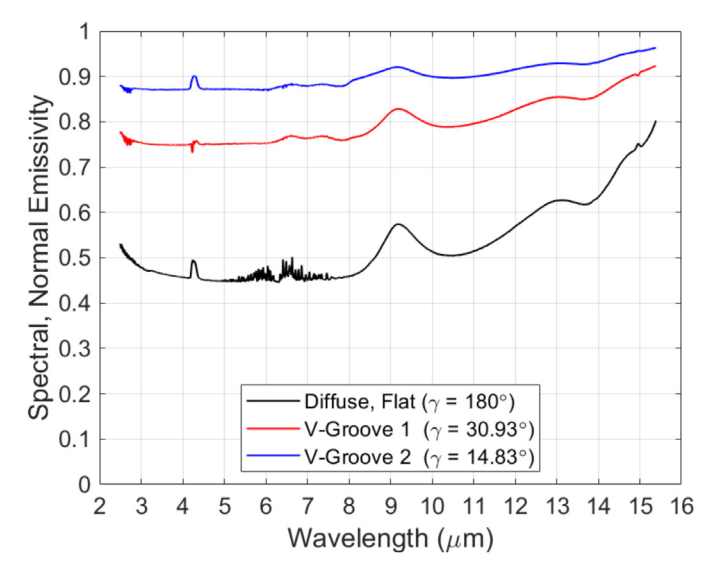


Fig. 9. Comparison of the spectral, normal emissivity for each sample. The average percent uncertainty of the flat, nearly diffuse sample is 4.20%, with maximum and minimum uncertainties of 7.73% and 3.04%, respectively. The average percent uncertainty of V-groove 1 is 1.13%, with maximum and minimum uncertainties of 1.75% and 0.95%, respectively. The average percent uncertainty of V-groove 2 is 0.93%, with maximum and minimum uncertainties of 1.55% and 0.77%, respectively.

consequence of the interference between the oxide film and metal substrate [37].

3.2. Effects of geometry on directional emissivity at a given wavelength

The directional emissivity of each sample is shown in Fig. 10. Data in these plots are obtained at a wavelength of 10.38 μm , which was found to be the wavelength corresponding to the most diffuse directional emissivity of the flat, nearly diffuse sample, outside of wavelength bands associated with gas absorption. This diffuse nature is demonstrated quantitatively by the standard deviation of emissivity over θ at $\phi=90^\circ$. As noted in Section 2.2.4, the standard deviation of this directional emissivity measurement at 10.38 μm is very small (<0.02; only 4.2% of the average emissivity over θ at $\phi=90^\circ$). Further, uncertainty in the presented data is sufficiently small that the error bars would interfere with interpreting neighboring data points and, therefore, are not provided on the plots. However, average and minimum/maximum uncertainties are summarized in the figure caption.

The flat, nearly diffuse sample varies little over θ and ϕ , with differences in directional emissivity essentially within the uncertainty of the measurement. This is to be expected given the diffuse nature of oxidized copper (with top surface cut by wire EDM) and the chosen wavelength, as described above. In the case of Vgroove 1 and 2 samples, directional effects begin to be observed due to the angular nature of the surfaces as compared to the flat, nearly diffuse sample. In particular, both V-groove samples demonstrate increasing directional emissivity with decreasing ϕ , for any given θ . Note that, at $\phi = 0^{\circ}$, no data for $\theta = 80^{\circ}$ is reported. For $\phi=0^{\circ}$, the observation path of the parabolic mirror is aligned with the axis of the V-groove, effectively seeing through the length of the V-groove. At these shallow angles, variability in the emissivity was high as the measured signal is comprised, in part, of empty space between V-groove peaks, resulting in large uncertainty. For this reason, data at $\theta=80^\circ$ was excluded for the case of $\phi=0^\circ$, only.

For the V-groove samples, which exhibit directional dependence, an increase in directional emissivity is observed with de-

creasing θ (towards the normal direction), for any given ϕ . Additionally, we observe that the directional emissivity distribution as a function of θ at $\phi = 60^{\circ}$ and $\phi = 90^{\circ}$ are in close agreement for both V-groove samples, with an average percent difference of 1.08% and maximum percent difference of 2.24% (for V-groove 1 with $\gamma = 30.93^{\circ}$). By comparison, when considering the directional emissivity distribution as a function of θ at $\phi = 90^{\circ}$ and $\phi = 0^{\circ}$, the average percent difference is 6.55%, with a maximum difference of 17.60% (for V-groove 1 with $\gamma = 30.93^{\circ}$). These results not only indicate that ϕ dependence deceases as ϕ approaches 90°, but that even in the most extreme comparison (e.g. when $\phi = 90^{\circ}$ or $\phi = 0^{\circ}$), the ϕ dependence of the V-groove samples is relatively small. This small dependence of directional emissivity on ϕ is further demonstrated by comparing the emissivity values over all ϕ at $\theta = 60^{\circ}$ for V-groove 1 sample, where the average emissivity is 0.72, the maximum is 0.79 (10.71% increase), and the minimum is 0.66 (7.20% decrease). These comparisons reveal a relatively low variation in directional emissivity over ϕ despite the obvious pattern associated with a corrugated surface. Note that these results are specific to the nature of the surface reflection which, for this case, is diffuse in nature for the wire EDM cut and fully oxidized surface.

Finally, even with V-grooves comprised of nearly diffuse interior surfaces (as indicated by Fig. 10a), a 27% decrease in spectral directional emissivity for V-groove 1 and 17% decrease for V-groove 2 are observed between $\theta=0^\circ$ and $\theta=80^\circ$ (for $\phi=90^\circ$), demonstrating directional dependence with θ in apparent surface emittance. When comparing across all samples (Fig. 10a-c), an average percent increase of 67.5% in directional emissivity was observed as the V-groove angle decreased from 180° to 14.83° (increase of 41.4% when the V-groove angle is decreased from 180° to 30.93°). This behavior, which was also observed in Fig. 9, is consistent with the behavior of a V-groove in that the surface behaves more like a blackbody.

3.3. Effects of geometry on total, directional emissivity

The spectral, directional emissivity of each sample surface, numerically integrated over the entire measured wavelength range (2.5 to 15.4 μ m) using Eq. (13), is shown in Fig. 11. These plots approximate the total, directional emissivity even though they do not span all wavelengths due to the majority of the blackbody emissive power distribution being contained between 2.5 to 15.4 μ m at this temperature (as shown in Fig. 7). Uncertainty in the presented data is again so small that the error bars would interfere with interpreting neighboring data points and, therefore, are not provided on the plots. However, average and minimum/maximum uncertainties are summarized in the figure caption.

When comparing Figs. 10 and 11 (at a given wavelength and averaged over all measured wavelengths), it is readily apparent that there are significant similarities. Although Fig. 11a indicates slightly less diffuse behavior for the flat sample when averaging over all wavelengths (as compared to that observed at 10.38 µm, Fig. 10), it is clear that the sample is still observably exhibiting diffuse behavior over the measured spectral range. This diffuse behavior is confirmed quantitatively by a low average standard deviation (<0.02) of the total, directional emissivity over all θ at $\phi=90^\circ$. This small standard deviation represents a small variation in emissivity over θ , characteristic of a nearly diffuse surface. Similar trends as noted in Section 3.2 apply; an increase in total, directional emissivity is observed with decreasing V-groove angle γ (Fig. 11a-c) and with decreasing θ (towards the surface normal), for both V-groove samples.

Despite the similarities mentioned, a notable difference is present in the directional emissivities reported in Figs. 10 and 11. In particular, the reported total, directional emissivity is lower than

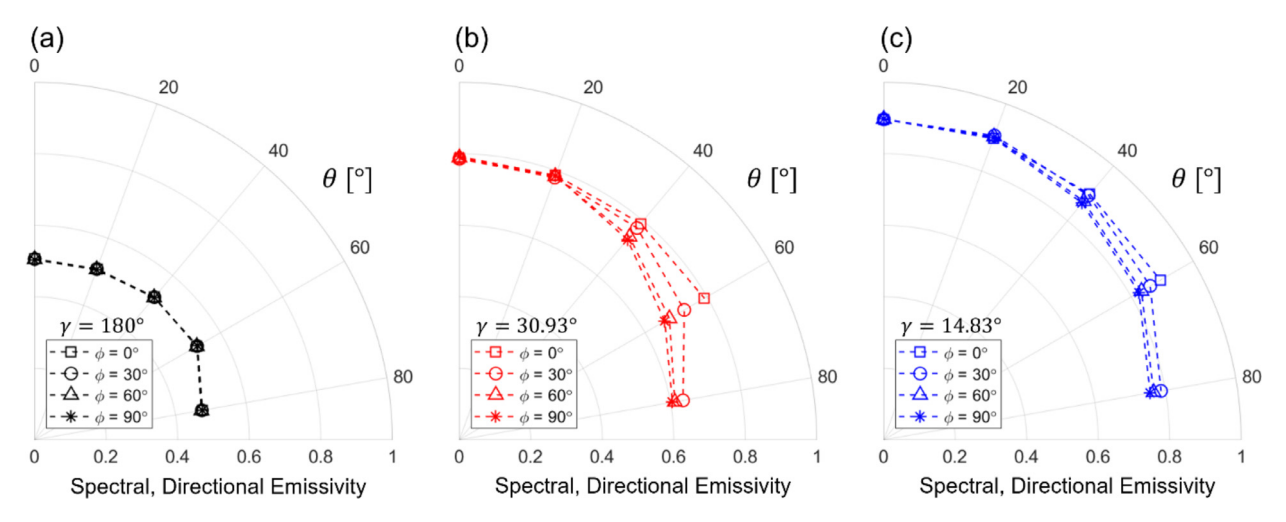


Fig. 10. Directional emissivity of the (a) flat, nearly diffuse (b) V-groove 1 and (c) V-groove 2 samples at the wavelength exhibiting the most diffuse behavior (10.38 μm). The average percent uncertainty of the flat, nearly diffuse sample is 3.42%, with maximum and minimum uncertainties of 4.26% and 2.85%, respectively. The average percent uncertainty of V-groove 1 is 2.00%, with maximum and minimum uncertainties of 4.83% and 0.87%, respectively. The average percent uncertainty of V-groove 2 is 0.94%, with maximum and minimum uncertainties of 1.81% and 0.73%, respectively.

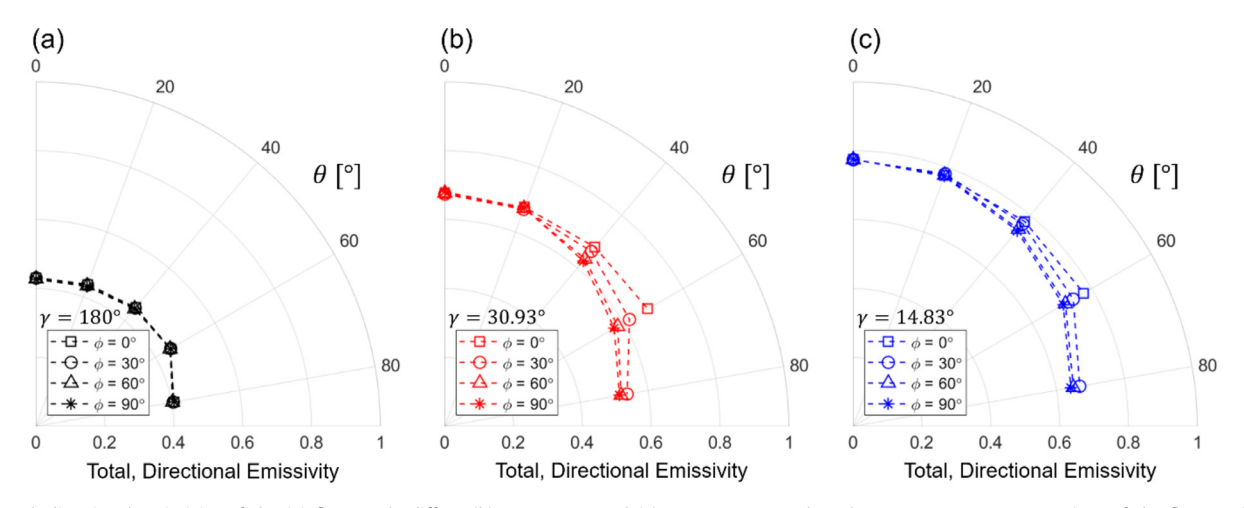


Fig. 11. Total, directional emissivity of the (a) flat, nearly diffuse (b) V-groove 1 and (c) V-groove 2 samples. The average percent uncertainty of the flat, nearly diffuse sample is 5.51%, with maximum and minimum uncertainties of 6.30% and 4.74%, respectively. The average percent uncertainty of V-groove 1 is 2.19%, with maximum and minimum uncertainties of 4.41% and 1.27%, respectively. The average percent uncertainty of V-groove 2 is 1.50%, with maximum and minimum uncertainties of 2.27% and 1.25%, respectively.

that for the directional emissivity at 10.38 μm in a given direction. This is consistent with expectations considering that most of the measured spectral range is below 10.38 μm , and the emissivity is observed to be generally lower at shorter wavelengths (see also Fig. 9).

3.4. Effects of geometry and wavelength on spectral, directional emissivity

The spectral, directional emissivity of each sample, at a constant value of $\phi=90^\circ$, is shown in Fig. 12. In particular, Fig. 12 illustrates the change in spectral, directional emissivity at different wavelengths across the measured spectral range, with uncertainties provided again in the figure caption. As expected, the same trend of increasing spectral, directional emissivity is observed with decreasing V-groove angle γ (Fig. 12a-c). Additionally, the higher emissivity trends observed in Fig. 9 at higher wavelengths can be seen in all three sample results, with V-groove 2 demonstrating particularly high emissivity values at a wavelength of 14 μ m. This is quantitatively demonstrated in achieving a spectral directional emissivity, averaged over θ , of 0.90, only \sim 10% below an ideal blackbody ($\phi=90^\circ$, $\lambda=14~\mu$ m). Strong agreement is seen in all

three plots at 4 and 8 μ m, with the increased emissivity values of 11 μ m once again following observed trends demonstrated by a percent increase in average spectral, directional emissivity over all θ of 5.61%. It is worth noting that the flat, nearly diffuse sample has the largest gap in emissivity values between wavelengths, with the gap growing smaller as the surface folds. This is seen graphically by comparing Fig. 12a–c, and indicates the same trend noted in Section 3.1, namely that spectral dependence decreases with decreasing V-groove angle γ . Once again, the flat, nearly diffuse sample exhibits a diffuse distribution, with much greater variance in emissivity values over θ observed in both folded samples.

4. Discussion

In Section 3.1, we observed that for each sample, higher spectral, normal emissivity values corresponded to longer wavelengths. In fact, the highest measured spectral, normal emissivities for the flat, V-groove 1, and V-groove 2 samples were 0.80, 0.92, and 0.96, respectively, which all corresponded to the highest wavelength in the measurement range (15.4 μ m). This was further demonstrated in section 3.4, where the highest emissivity distribution (over θ at $\phi = 90^{\circ}$) for each sample corresponded to a wavelength of 15 μ m.

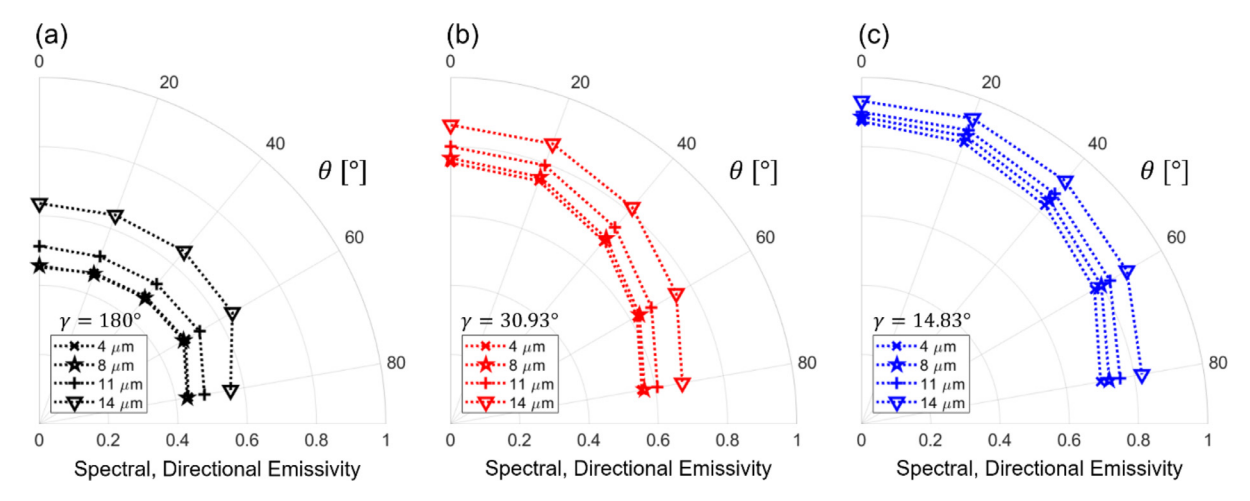


Fig. 12. Spectral, directional emissivity at $\phi = 90^{\circ}$ of the (a) flat, nearly diffuse (b) V-groove 1 and (c) V-groove 2 samples. The average percent uncertainty of the flat, nearly diffuse sample is 3.85%, with maximum and minimum uncertainties of 5.35% and 2.69%, respectively. The average percent uncertainty of V-groove 1 is 2.53%, with maximum and minimum uncertainties of 4.82% and 1.02%, respectively. The average percent uncertainty of V-groove 2 is 1.17%, with maximum and minimum uncertainties of 2.09% and 0.69%, respectively.

In the case of the V-groove 2 sample, an average (over θ) emissivity value of 0.94 was reported, just 6.4% below an ideal blackbody emissivity of 1. Given that this trend is observed for the flat, nearly diffuse sample, the data supports the condition that the surfaces are comprised of oxidized copper that are diffuse in nature. This result is not due to the changing geometry of the sample but rather is specific to the interior testing surface (which may differ for a given application).

Of greater interest are the trends regarding γ observed in Sections 3.1 and 3.4, namely that the spectral dependence of apparent emissivity for corrugated surfaces decreases with decreasing V-groove angle γ . This decrease in spectral dependence is demonstrated graphically in the flattening of the spectral, normal emissivity plots as γ decreases (Fig. 9) as well as the shrinking gap between spectral, directional distributions (Fig. 12) with decreasing V-groove angle. It implies that the wavelength dependence of the interior surface has less influence on the amount of emitted or absorbed thermal radiation as the V-groove angle γ decreases, despite the strong spectral dependence observed for the intrinsic surface emissivity of the flat, nearly diffuse sample (Fig. 9). Such findings could play a critical role in future thermal control designs, such as the selection of radiator interior surface finishes.

Another important observation can be made by examining the results of Section 3.2, regarding the distribution of emissivity values over ϕ at a constant θ value of 60°. It was found that emissivity dependence on ϕ is small, shown by the maximum emissivity being only 10.71% higher than the average emissivity over this range. In most applications, this is likely a negligible difference, one that may not warrant the additional work required to make measurements over ϕ . However, with the magnitude of this dependence now quantified, designers now have this dependence quantified and can make decisions regarding how to utilize preferred directions of emission to control radiative heat transfer. Nevertheless, such small ϕ dependence is not necessarily characteristic of all corrugated surfaces and may differ for specific design cases (e.g. possibly for specular surfaces). Regardless, the measurement methodology and experimental design presented here provide a foundation for future studies of the spectral, directional emissivity of angular/origami surfaces.

On the other hand, strong directional dependence on θ was observed in the results presented in Sections 3.2 and 3.2. At the wavelength corresponding to the most diffuse directional emissivity of the flat sample (10.38 µm), large percent decreases in emis-

sivity of 27% for V-groove 1 and 17% for V-groove 2 were observed between $\theta = 0^{\circ}$ and $\theta = 80^{\circ}$. These results were specific to $\phi = 90^{\circ}$, with directional dependence on θ actually decreasing as ϕ approached 0°. In fact, the most diffuse distribution for Vgroove 1 and 2 corresponded to $\phi = 0^{\circ}$. This trend (directional dependence on θ increasing as $\phi \to 90^\circ$) was also present in the results of Section 3.3 for both V-grooves, indicating that this trend is not specific to $\lambda = 10.38 \mu m$, but rather is general to the entire measured wavelength range. These finding, which quantify the directional dependence of the apparent emissivity of a corrugated surface, allow one to control or affect net radiative heat transfer by the orientation of the apparent surface relative to other bodies/surfaces. This is especially critical in spacecraft applications, where the absence of convection and conduction cause greater dependence on the radiative heat transfer exchange between the craft and other vessels/celestial bodies.

One final noteworthy trend observed in the results is the increase in apparent emissivity with decreasing V-groove angle. For example, in Section 3.2, an average percent increase of 67.5% in directional emissivity was observed as the V-groove angle decreased from 180° to 14.83°. Even though directional dependence is still present, the high emissivity values and aforementioned decrease in spectral dependence indicate that the surface is approaching blacklike behavior with decreasing V-groove angle γ . This result, which is an excellent demonstration of the cavity effect, underscores the capability of corrugates surfaces to provide variable thermal control through the variable geometric positioning. This finding, combined with the experimental quantification of the directional and spectral dependence of the folding apparent surface, enable designers to utilize preferred directions of emission and absorption, as well as the geometry of the surface itself, to control radiative heat transfer.

5. Conclusion

In this work, a method to measure directional surface quantities over the hemisphere of a corrugated surface was developed. The spectral, normal emissivity of fully oxidized copper over the wavelength range of 2.5 to 15.4 μ m was measured, along with the spectral, directional emissivity of a fully oxidized, copper corrugated surface over the same wavelength range. For the surfaces tested, we observe that (1) higher emissivity values correspond to higher wavelengths in the spectral range of 2.5 to 15.4 μ m, (2) apparent

emissivity values increase with decreasing V-groove angle resulting in less spectral variation in emissivity and greater blackbody like behavior, (3) azimuth dependence can be relatively small despite the obvious pattern associated with a corrugated surface, (4) as the V-groove angle decreases, higher emissivity values are associated with $\theta\!\to\!0^\circ$ and $\phi\!\to\!90^\circ$. The quantified spectral, directional dependence of the apparent emissivity combined with the variation in apparent emissivity observed with changes in V-groove angle provide a foundation for further design and utilization of collapsible radiators in thermal control of spacecraft as well as all other applications where thermal radiation plays a major role in heat exchange with the surroundings.

Declaration of Competing Interest

The authors declare that they have no known competing financial interests or personal relationships that could have appeared to influence the work reported in this paper.

The authors declare the following financial interests/personal relationships which may be considered as potential competing interests:

Brian Iverson reports financial support was provided by National Science Foundation.

CRediT authorship contribution statement

Kyle S. Meaker: Conceptualization, Formal analysis, Investigation, Methodology, Validation, Visualization, Writing – original draft. **Ehsan Mofidipour:** Validation, Visualization, Writing – review & editing. **Matthew R. Jones:** Conceptualization, Methodology, Writing – review & editing. **Brian D. Iverson:** Conceptualization, Funding acquisition, Methodology, Supervision, Writing – review & editing.

Data availability

Data will be made available on request.

Acknowledgments

This material is based upon work supported by the National Science Foundation (grant number 1749395).

Supplementary materials

Supplementary material associated with this article can be found, in the online version, at doi:10.1016/j.ijheatmasstransfer. 2022.123745.

References

- [1] J.R. Cannon, B.D. Iverson, W. Song, R.B. Mulford, Passively actuated, triangular radiator fin array, NASA Thermal and Fluid Analysis Workshop, August 18-20, 2020, (virtual conference), 2020.
- [2] D.G. Gilmore, Spacecraft Thermal Control Handbook, 2nd ed., The Aerospace Corporation Press, El Segundo, CA, 2002.
- [3] L.M. Grob, T.D. Swanson, Parametric study of variable emissivity radiator surfaces, in: AIP Conference Proceedings, 504, 2000, pp. 809–814, doi:10.1063/1.
- [4] H. Nagano, A. Ohnishi, Y. Nagasaka, Development of a lightweight deployable/stowable radiator for interplanetary exploration, Appl. Therm. Eng. 31 (2011) 3322–3331, doi:10.1016/j.applthermaleng.2011.06.012.
- [5] R. Ponnappan, J.E. Beam, E.T. Mahefkey, Roll-out-fin expandable space radiator concept, J. Thermophys. Heat Transfer 2 (1988) 91.
- [6] C. Bertagne, P. Walgren, L. Erickson, R. Sheth, J. Whitcomb, D. Hartl, Coupled behavior of shape memory alloy-based morphing spacecraft radiators: Experimental assessment and analysis, Smart Mater. Struct. 27 (2018) 065006, doi:10.1088/1361-665X/aabbe8.
- [7] N. Athanasopoulos, N.J. Siakavellas, Smart patterned surfaces with programmable thermal emissivity and their design through combinatorial strategies, Sci. Rep. 7 (2017) 1–30, doi:10.1038/s41598-017-13132-6.

- [8] R.B. Mulford, S.D. Salt, L.P. Hyatt, K.S. Meaker, V.H. Dwivedi, M.R. Jones, B.D. Iverson, Experimental demonstration of heat loss and turn-down ratio for a multi-panel, actively deployed radiator, Appl. Therm. Eng. 178 (2020) 115658, doi:10.1016/j.applthermaleng.2020.115658.
- [9] B.D. Iverson, R.B. Mulford, E.T. Lee, M.R. Jones, Adaptive net radiative heat transfer and thermal management with origami-structured surfaces, in: Proceedings of the 16th International Heat Transfer Conference, August 10-15, 2018. Beiling, China. 2018.
- [10] M.J. Blanc, R.B. Mulford, M.R. Jones, B.D. Iverson, Infrared visualization of the cavity effect using origami-inspired surfaces, J. Heat Transf. 138 (2016).
 [11] R.B. Mulford, M.R. Jones, B.D. Iverson, Dynamic Control of Radiative Surface
- [11] R.B. Mulford, M.R. Jones, B.D. Iverson, Dynamic Control of Radiative Surface Properties With Origami-Inspired Design, J. Heat Transf. 138 (2016), doi:10. 1115/1.4031749.
- [12] R.B. Mulford, V.H. Dwivedi, M.R. Jones, B.D. Iverson, Control of net radiative heat transfer with a variable-emissivity accordion tessellation, J. Heat Transf. 141 (2019), doi:10.1115/1.4042442.
- [13] R.B. Mulford, N.S. Collins, M.S. Farnsworth, M.R. Jones, B.D. Iverson, Total hemispherical apparent radiative properties of the infinite V-groove with specular reflection, Int. J. Heat Mass Transf. 124 (2018), doi:10.1016/j.ijheatmasstransfer. 2018.03.041.
- [14] C. Da Wen, I. Mudawar, Emissivity characteristics of polished aluminum alloy surfaces and assessment of multispectral radiation thermometry (MRT) emissivity models, Int. J. Heat Mass Transfer 48 (2005) 1316–1329, doi:10.1016/j. ijheatmasstransfer.2004.10.003.
- [15] C. Da Wen, I. Mudawar, Emissivity characteristics of roughened aluminum alloy surfaces and assessment of multispectral radiation thermometry (MRT) emissivity models, Int. J. Heat Mass Transf. 47 (2004) 3591–3605, doi:10.1016/j. iiheatmasstransfer.2004.04.025.
- [16] Z. Yuan, K. Yu, L. Li, G. Wang, K. Zhang, Y. Liu, New directional spectral emissivity measurement apparatus simultaneously collecting the blackbody and sample radiation, Rev. Sci. Instrum. 93 (2022), doi:10.1063/5.0073459.
- [17] L. Li, K. Yu, K. Zhang, Y. Liu, F. Zhang, Y. Liu, Accuracy improvement for directional polarized spectral emissivity measurement in the wavelength range of 4–20 µm, Exp. Therm. Fluid Sci. 125 (2021) 110379, doi:10.1016/j. expthermflusci.2021.110379.
- [18] I. González de Arrieta, T. Echániz, R. Fuente, E. Rubin, R. Chen, J.M. Igartua, M.J. Tello, G.A. López, Infrared emissivity of copper-alloyed spinel black coatings for concentrated solar power systems, Sol. Energy Mater. Sol. Cell. 200 (2019) 109961, doi:10.1016/j.solmat.2019.109961.
- [19] V.V. Vitkovskii, V.G. Gorshenev, Y.F. Potapov, Measurement of spectral directional emissivity of materials and coatings in the infrared region of spectrum, Therm. Eng. 56 (2009) 245–248, doi:10.1134/S0040601509030100.
- [20] T. Fu, M. Duan, J. Tang, C. Shi, Measurements of the directional spectral emissivity based on a radiation heating source with alternating spectral distributions, Int. J. Heat Mass Transf. 90 (2015) 1207–1213, doi:10.1016/j. ijheatmasstransfer.2015.07.064.
- [21] G. Feng, Y. Wang, Y. Li, J. Zhu, L. Zhao, Greatly enhanced infrared normal spectral emissivity of microstructured silicon using a femtosecond laser, Mater. Lett. 65 (2011) 1238–1240, doi:10.1016/j.matlet.2011.01.067.
- [22] I. Setién-Fernández, T. Echániz, L. González-Fernández, R.B. Pérez-Sáez, M.J. Tello, Spectral emissivity of copper and nickel in the mid-infrared range between 250 and 900 C, Int. J. Heat Mass Transf. 71 (2014) 549–554, doi:10. 1016/j.ijheatmasstransfer.2013.12.063.
- [23] P. Herve, J. Cedelle, I. Negreanu, Infrared technique for simultaneous determination of temperature and emissivity, Infrared Phys. Technol. 55 (2012) 1–10, doi:10.1016/j.infrared.2010.09.001.
- [24] C. Da Wen, T.Y. Chai, Experimental investigation of emissivity of aluminum alloys and application of multispectral radiation thermometry, Appl. Therm. Eng. 31 (2011) 2414–2421, doi:10.1016/j.applthermaleng.2011.04.005.
- [25] D. Shi, Y. Liu, J. Sun, Z. Zhu, H. Liu, A new experimental apparatus for measurement of spectral emissivity of opaque materials using a reflector as the dummy light source, Int. J. Heat Mass Transf. 55 (2012) 3344–3348, doi:10. 1016/j.ijheatmasstransfer.2012.02.055.
- [26] C.Da Wen, Investigation of steel emissivity behaviors: Examination of Multi-spectral Radiation Thermometry (MRT) emissivity models, Int. J. Heat Mass Transf. 53 (2010) 2035–2043, doi:10.1016/j.ijheatmasstransfer.2009.12.053.
- [27] T.J. Moore, M.R. Jones, D.R. Tree, R. Daniel Maynes, L.L. Baxter, An experimental method for making spectral emittance and surface temperature measurements of opaque surfaces, J. Quant. Spectrosc. Radiat. Transf. 112 (2011) 1191–1196, doi:10.1016/j.jqsrt.2010.08.020.
- [28] T.J. Moore, D.P. Cundick, M.R. Jones, D.R. Tree, R.D. Maynes, L.L. Baxter, In situ measurements of the spectral emittance of coal ash deposits, J. Quant. Spectrosc. Radiat. Transf. 112 (2011) 1978–1986, doi:10.1016/j.jqsrt.2011.04.013.
- [29] M. Modest, Radiative Heat Transfer, 3rd ed., Academic Press, Amsterdam, 1993.
- [30] P. Wang, Z. Hu, Z. Xie, M. Yan, A new experimental apparatus for emissivity measurements of steel and the application of multi-wavelength thermometry to continuous casting billets, Rev. Sci. Instrum. 89 (2018), doi:10.1063/1. 5007225.
- [31] K. Yu, R. Tong, K. Zhang, Y. Liu, Y. Liu, An Apparatus for the directional spectral emissivity measurement in the near infrared band, Int. J. Thermophys. 42 (2021), doi:10.1007/s10765-021-02813-0.
- [32] G. Teodorescu, P.D. Jones, Spectral and directional emittance of alumina at 823 K, J. Mater. Sci. 43 (2008) 7225–7229, doi:10.1007/s10853-008-2945-y.
- [33] Y.M. Guo, S.J. Pang, Z.J. Luo, Y. Shuai, H.P. Tan, H. Qi, Measurement of directional spectral emissivity at high temperatures, Int. J. Thermophys. 40 (2019), doi:10.1007/s10765-018-2472-2.

- [34] L. Del Campo, R.B. Prez-Sáez, X. Esquisabel, I. Fernández, M.J. Tello, New experimental device for infrared spectral directional emissivity measurements in a controlled environment, Rev. Sci. Instrum. 77 (2006), doi:10.1063/1.2393157.
- (2016) Got: 10. 1063 J. 1.2393157.
 [35] R.B. Mulford, N.S. Collins, M.S. Farnsworth, M.R. Jones, B.D. Iverson, Total hemispherical apparent radiative properties of the infinite V-Groove with diffuse reflection, J. Thermophys. Heat Transf. 32 (2018) 1108–1112, doi:10.2514/1.T5485.
 [36] R.B. Mulford, M.R. Jones, B.D. Iverson, Heat transfer, efficiency and turn-down
- [36] R.B. Mulford, M.R. Jones, B.D. Iverson, Heat transfer, efficiency and turn-down ratio of a dynamic radiative heat exchanger, Int. J. Heat Mass Transf. 143 (2019) 118441, doi:10.1016/j.ijheatmasstransfer.2019.118441.
- [37] K. Yu, H. Zhang, Y. Liu, Y. Liu, Study of normal spectral emissivity of copper during thermal oxidation at different temperatures and heating times, Int. J. Heat Mass Transf. 129 (2019) 1066–1074, doi:10.1016/j.ijheatmasstransfer.2018. 09 116
- [38] T.L. Bergman, A.S. Lavine, F.P. Incropera, D.P. DeWitt, Fundamentals of Heat and Mass Transfer, 7th ed., Wiley, Hoboken, NJ, 2011.
 [39] P.S. Wei, H.H. Chiu, Y.C. Hsieh, D.L. Yen, C. Lee, Y.C. Tsai, T.C. Ting, Absorp-
- [39] P.S. Wei, H.H. Chiu, Y.C. Hsieh, D.L. Yen, C. Lee, Y.C. Tsai, T.C. Ting, Absorption coefficient of water vapor across atmospheric troposphere layer, Heliyon 5 (2019) e01145, doi:10.1016/j.heliyon.2019.e01145.